Design and Optimization of a Wave Energy Converter for Drifting Sensor Platforms in Realistic Ocean Waves

Julius Harms[a,1,*], Marten Hollm[b,1,*], Leo Dostal[b,*], Thorsten A. Kern[a], Robert Seifried[b]

[a] *Institute for Mechatronics in Mechanics, Hamburg University of Technology, 21073 Hamburg, Germany*
[b] *Institute of Mechanics and Ocean Engineering, Hamburg University of Technology, 21073 Hamburg, Germany*

Abstract

One of the biggest challenges in converting wave energy is to enable the use of low frequency waves, since the highest waves in typical sea states have low frequencies, as can be seen from the corresponding wave spectra, such as the Pierson-Moskowitz or JONSWAP spectra. In this paper, we show that this challenge is indeed achievable for the operation of small autonomous drifting sensor platforms. We present the design and optimization of a compact wave energy converter that freely floats in random sea waves. An optimization of the dynamical behavior as well as the electromagnetic power take-off is conducted based on simulations and experiments. The platform has compact dimensions of 50 cm draft and 50 cm diameter, which leads to special requirements for size and appearance. To meet these requirements, a two-body self-reacting point absorber is designed and a flux switching permanent magnet linear machine is developed for the power take-off. The developed system is validated by experiments in a wave flume and the linear generator is analyzed on a test bench. A coupled model is used to simulate and optimize the corresponding mechanical system, which leads to an increased output power from below 10 mW for the simulated initial setup to a power output of more than 100 mW in the simulation. Simulations and experiments

*Corresponding authors
Email addresses: julius.harms@tuhh.de (Julius Harms), marten.hollm@tuhh.de (Marten Hollm), dostal@tuhh.de (Leo Dostal)
[1] Equal contribution

are performed for regular and random waves in order to provide realistic approximations of the total output power.

Keywords: Wave Energy Converter, Linear Generator, Drifter, energy harvesting, SRPA, FSPMLM

1. Introduction

As the climate crisis progresses, high-resolution climate models and reliable in situ measurement data from the ocean become more and more vital to us. One possibility to obtain measurement data with high spatial resolution is to use low-cost sensor Drifters. These relatively small sensor platforms (Fig. 1) are deployed in large quantities in the ocean in order to observe ocean currents and collect measurement parameters that are valuable for marine science and meteorology. As instrumentation increases, so do the power requirements of these sensor Drifters. Drifters powered only by batteries have a limited life span, which requires long-term applications that span months and even years to take advantage of energy harvesting [1]. While solar energy is a common choice for drifting sensor platforms, wave energy with its high availability becomes particularly interesting for long-term applications of small platforms with little space for solar panels or for applications in polar regions with limited sunlight. In the scope of this work, the Drifter design shown in Fig. 1 is extended by a wave energy converter (WEC) for ocean Drifters.

(a) (b) (c)

Figure 1: a: Deployed multi-sensor Drifter swimming in the water; b: Drifter in the air before deployment; c: 3D model of a Drifter with annotations.

1.1. State of the Art

The conversion of ocean energy is becoming increasingly relevant as a renewable energy source. A particular interest is addressed to large WECs used in big power plants [2] but due to its high availability, ocean wave energy harvesting is more and more considered in the field of ocean monitoring. Underwater glider are autonomous underwater vehicles (AUVs) that demonstrate potential methods of energy harvesting in the ocean. A prominent example is the wave glider [3], which uses wave energy for its propulsion. Other gliders use various methods of kinetic [4] or thermal [5] energy harvesting. Moored sensor buoys, used to monitor fixed offshore points, can use the concept of a point absorber, where the mooring line is used as a rigid reference point, allowing to harvest large amounts of energy from the relative motion in the wave [6].

In this paper, we are concerned with freely drifting sensor buoys without mooring as a rigid reference. One example is a ball-shaped wave Drifter, for which different means of kinetic energy harvesting were developed. Carandell et al. [7] first presented a small kinetic energy harvester based on a gyro pendulum and later presented a different approach of a rolling mass energy harvester [8]. Similar approaches are presented by Shi et al. [9] using piezoelectric vibrational energy harvesting and Li et al. [10] using a swing body mechanism. Spherical Drifters are more suitable for wave studies and near-shore applications [11]. Drifters for surface current measurements, such as those discussed in this paper, require a drogue (Fig. 1c) to reduce wind- and wave-induced influence [12, 13]. The drogue serves as a sail in the water current and has a stabilizing effect, which significantly reduces the platform roll. The relationship between the electrical output and the pitch degree of freedom was studied by Rodrigues et al. [14] who investigated triboelectric nanogenerators for kinetic wave energy harvesting. A significant dependency of the platforms dynamics on the power output indicates that kinetic energy harvesting from rolling might be a good solution for buoys but is much less efficient for an upright sensor Drifter with drogue.

Other energy harvesting concepts for upright floating sensor buoys make use of the relative motion in the water. Joe et al. [15] implemented a self-rectifying wave-induced turbine below the water surface which is powered from the up and down motions in the waves. A similar concept was applied to a Drifter of the Surface Velocity Program (SVP) [16] by Wu et al. [1]. In that work it is shown that a counter-rotating wave energy converter can be used to power a small scale drifting sensor buoy. The presented pre-

vious works require a comparably high constructional effort, which hinders a cost-effective manufacturing and the exposed turbines and rotors can be susceptible to contamination.

In this paper, we propose a novel, low-cost approach for wave energy harvesting on mooringless sensor buoys by applying a minimalistic concept of a self-reacting point absorber (SRPA) [17] to the sensor Drifter. The SRPA is a two-body system for wave energy conversion that requires relative motion between the buoy and the drogue, which then both act as float and reacting body respectively. Numerous experimental and simulative studies have been conducted to investigate the hydrodynamic excitation forces acting on the plate and buoy, see for example [17, 18, 19, 20]. The corresponding motion of the two components was analyzed with reduced complexity. Most simulations and experiments so far have been performed for regular waves and the considered mechanical system has been studied only in larger dimensions and power classes, e.g. [17, 21, 22].

The power take-off of the WEC can be implemented by an electrical generator in the buoy. Since the motion of an SRPA is linear, a direct-drive linear generator has the great advantage of a simple design and implementation. A transmission of the motion into a rotation is not considered to reduce complexity and a direct-drive linear generator is developed. Linear generators for kinetic wave energy harvesting use various generator concepts, but the functionality at low translation speeds and high thrust forces is a critical design factor [23]. To provide a brief overview, a distinction can be made between three basic functional principles.

The **synchronous permanent magnet linear machine (SPMLM)** is most commonly used as a motor but can also function as a generator. In its special variant as a double-sided generator [24] or with Halbach array configuration [25], the machine can be specially adapted for wave energy conversion. With a SPMLM, the magnets are located on the translator, which increases the weight, constructional effort and costs of the translator, especially when being in Halbach configuration. With the aim for a simple and low-cost system, the placement of magnets and coils on the shorter armature - the stator- is therefore a more appropriate choice.

This is given by two other linear generators types considered here, the **variable reluctance linear machine (VRLM)** and the **flux switching permanent magnet linear machine (FSPMLM)**. The low efficiency of traditional VRLMs makes this design unsuitable for ocean environments that have high thrust force and low speed [26]. On the other hand, FSPMLMs

have the advantage of high switching frequencies at low translator speed and are therefore often used as WEC. The design principles for a flux switching machine were first introduced by Rauch et al. [27] and optimized in several publications on flux switching rotary machines [28, 29]. For linear applications, the FSPMLM is implemented as either a planar machine [30, 31], the related vernier hybrid machine [23] or as tubular machine [32, 33]. A tubular FSPMLM [34] is due to its high power density and efficiency superior to the planar linear structures [35]. Furthermore, the manufacturing of a tubular structure is more cost-efficient and the design is simple and easy to integrate into the Drifter's housing. Therefore, the concept of a tubular FSPMLM is selected and designed in the following.

In this paper, the concept of an SRPA is applied for the first time to a small sensor platform for energy harvesting. We discuss the problems of miniaturization and optimize both mechanical dynamics and electromagnetic energy conversion in order to overcome them. Simulations and a series of experiments are conducted for optimization and development. Since most previous studies have considered only the regular sea state, we also consider irregular seas for optimization in realistic wave conditions. The generator design is based on the concept of a FSPMLM and proposes a novel pole and stator arrangement that allows sufficient voltage values even at small amplitudes and low frequencies. The objective of this paper is to present the design and optimization of a compact and low-cost WEC based on the concept of an SRPA, which meets the dimensions and requirements of a small ocean Drifter, in irregular seas.

1.2. System Requirements and Application

Ongoing development of a low-cost multi-sensor platform [36, 37] shows that typical average power demands of a Drifter ranges from 10mW (GPS -tracking every 5 minutes) to above 100mW (multiple sensors and satellite transmission every 5 minutes). The size of a Drifter depends on its application. The dimensions for low-cost platforms are essentially limited to allow good handling, while deploying large quantities from a ship. Established solutions show a diameter of 20 cm to 40 cm for the floating buoy and an immersion depth of 40 cm to 60 cm [38, 13]. The lower part of the Drifter, the drogue, has a vertical cross-section of about 40 cm. To keep the Drifter affordable for massive deployments, the design should follow a simplistic approach. The WEC to be developed should therefore be simple and cost-effective.

1.3. Outline

The content of this work is as follows: First, the equations of motion of the considered system are derived and validated through a series of experiments in section 2. Then a linear generator is designed and optimized for the electromagnetic power take-off of the WEC in section 3. The generator design is selected based on conceptual considerations and a parametric FEM simulation analysis. The generator is implemented and tested on a testbench to validate the FEM results and show the potential power output of the developed system. In section 4, the mechanical and electromagnetic model are coupled to allow optimization of the mechanical setup for different sea conditions. Thereby, the power output of the optimized system in irregular seas is estimated based on simulations. Finally, this work ends with a conclusion in section 5.

2. Modeling of a Two-Body Wave Energy Converter Excited by Water Waves

The Drifter design considered here is inspired by established designs for compact and affordable Drifter, such as CARTHE Drifter [38] or the Drifter of Meyerjürgens et al. [13]. The simplified adaptation of the design is shown in Fig. 2a and consists of a cylindrical buoy with a submerged circular plate, which replaces the Drifters drogue. The effects of the vertical plates on the drogue are not considered in this stage, since their influence on the vertical motion is small. Reducing the model complexity allows an analytic analysis of the construction, which leads to insights that can be taken into account in the design of the WEC-Drifter. Thereby, the pitch motion of the system is neglected and only the heave motion of the buoy and plate is considered. Both parts of this two-body wave energy converter are forced by respective hydrodynamic forces, which appear in the corresponding equations of motion and have to be calculated first.

2.1. Description of the Mechanical System

The buoy is located at the water surface and connected to the submerged plate by means of a connecting rod and a spring. The connection rod runs through the buoy and is also present above the water surface. The buoy, connection rod, and plate have a radius of R_b, R_c and R_p, respectively. The respected distances between the water surface and the lower boundary of the buoy, connection rod, and plate are b, e_1 and e_2. The coordinate

system (x, y, z) is located at the water surface in the absence of any water wave and the water depth is denoted by h. A sketch of the resulting two-body wave energy converter is shown in Fig. 2b. Due to an installed power take-off system, energy can be extracted from the relative motion between the floating and submerged body. This energy extraction induces electrical damping in the system. In combination with the mechanical friction, this overall damping is considered by means of a damper fixed between the two bodies. Thereby, a linear and nonlinear damping force is assumed. Fig. 2c visualises the resulting connection of the two bodies.

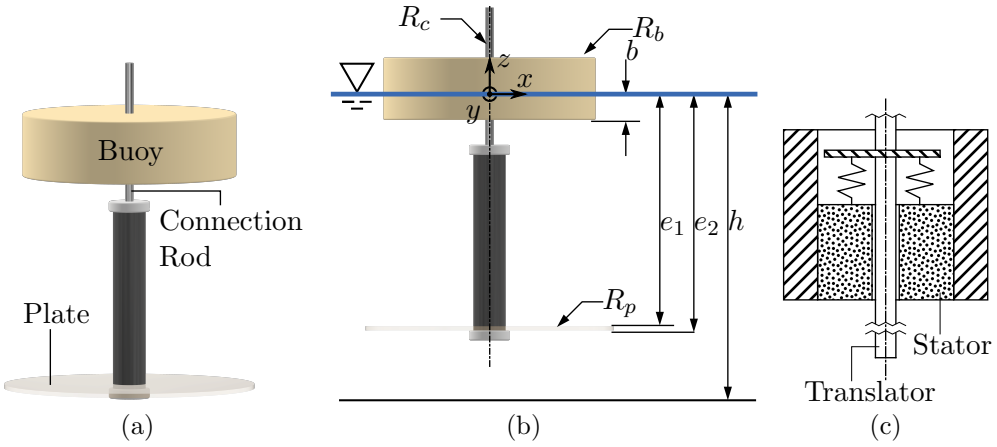

Figure 2: a: Simplified Drifter design for WEC-analysis with descriptions; b: Parameter names for the parameterised model of the two-body WEC; c: Concept sketch of the WEC buoy with spring and electromagnetic damping.

2.2. The Equations of Motion of the Mechanical System in Regular Waves

In order to gain first insights in the system dynamics, the pitch motion of the system is neglected and only the heave motion of the buoy and plate is considered. Then the corresponding equations of motion are given by

$$\begin{aligned} m_1\ddot{\xi}_1 &= -m_1 g + F_\mathrm{s} + F_\mathrm{d} - \lambda_{\mathrm{exp},1}\dot{\xi}_1 + \iint_{S_1} p(x,y,z,t) n_3 \mathrm{d}S, \\ m_2\ddot{\xi}_2 &= -m_2 g - F_\mathrm{s} - F_\mathrm{d} - \lambda_{\mathrm{exp},2}\dot{\xi}_2 + \iint_{S_2} p(x,y,z,t) n_3 \mathrm{d}S, \end{aligned} \tag{1}$$

whereby ξ_1 and ξ_2 are the respective heave displacement of the buoy and plate with respect to the equilibrium position in still water, at which ξ_1

and ξ_2 are zero; m_1 and m_2 are the respective masses of the buoy and the combination of the rod and the plate; S_1 and S_2 are the respective wetted surfaces of the buoy and plate; g is the acceleration due to gravity; p is the hydrodynamic pressure, which acts on the corresponding bodies; n_3 is the vertical normal vector, which points out of the fluid; F_s and F_d are the spring and damping forces, which are acting at the connection points; $\lambda_{\mathrm{exp},1}$ and $\lambda_{\mathrm{exp},2}$ are the respective tuning parameters, which are used in order to make simulation and experimental results comparable.

In this section, only regular waves are considered. For this, the water displacement of amplitude A, frequency ω and wave number k_e is given by

$$\eta(x,t) = \mathrm{Re}\{A\exp(\mathrm{i}(k_\mathrm{e}x - \omega t))\} \quad \text{with } \omega^2 = k_\mathrm{e} g \tanh(k_\mathrm{e} h). \tag{2}$$

In section 2.6, the system behavior is validated in a wave flume with a small water depth. Therefore, water depth h has been incorporated into Eq. 2, even though the mechanical system is deployed primarily in deep water. The computation of the corresponding pressure p is described in Appendix 1. Thereby, potential flow theory and the results of Olaya et al. [20] are used.

Using a linear stiffness force

$$F_s = F_0 + \kappa_\mathrm{s}(\xi_2 - \xi_1) \tag{3}$$

with stiffness constant κ_s, the equations of motion can be written as

$$\begin{bmatrix} m_1 + \mu_{1,1} & \mu_{2,1} \\ \mu_{1,2} & m_2 + \mu_{2,2} \end{bmatrix} \begin{pmatrix} \ddot{\xi}_1 \\ \ddot{\xi}_2 \end{pmatrix} + \begin{bmatrix} \lambda_{1,1} + \lambda_{\mathrm{exp},1} & \lambda_{2,1} \\ \lambda_{1,2} & \lambda_{2,2} + \lambda_{\mathrm{exp},2} \end{bmatrix} \begin{pmatrix} \dot{\xi}_1 \\ \dot{\xi}_2 \end{pmatrix} + \begin{bmatrix} \rho\pi g(R_\mathrm{b}^2 - R_\mathrm{c}^2) + \kappa_\mathrm{s} & -\kappa_\mathrm{s} \\ -\kappa_\mathrm{s} & \rho\pi g R_\mathrm{c}^2 + \kappa_\mathrm{s} \end{bmatrix} \begin{pmatrix} \xi_1 \\ \xi_2 \end{pmatrix} = \mathrm{Re}\left\{ \begin{bmatrix} A f_1 e^{-\mathrm{i}\omega t} \\ A f_2 e^{-\mathrm{i}\omega t} \end{bmatrix} \right\} + \begin{pmatrix} F_\mathrm{d} \\ -F_\mathrm{d} \end{pmatrix}. \tag{4}$$

In this equation, F_0 is the force of the spring at equilibrium in the absence of water waves; $\mu_{j,k}$ and $\lambda_{j,k}$ are the respective added mass coefficients and hydrodynamic damping coefficients for heave of body k resulting from a heave motion of body j, where $j,k \in \{1,2\}$; f_k is the hydrodynamic excitation force acting on body k, whereby $k \in \{1,2\}$. All added mass coefficients, hydrodynamic damping coefficients and hydrodynamic excitation forces depend on the geometry of the system, wave frequency ω and water depth h. For the computation of Eqs. (4), the balance of forces in z-direction in the absence of water waves has been incorporated:

$$m_1 g = \rho\pi g(R_\mathrm{b}^2 - R_\mathrm{c}^2)b + F_0, \quad m_2 g = \rho\pi g(R_\mathrm{p}^2(e_2 - e_1) + R_\mathrm{c}^2 e_1) - F_0. \tag{5}$$

The equations of motion (4) are a generalization of the equations found by Liang et al. [21], who have neglected the radius of the connection rod R_c. Moreover, they assumed that the submerged body is deployed far enough from the floating body and free surface such that the added masses ($\mu_{1,2}$, $\mu_{2,1}$) and the hydrodynamic damping ($\lambda_{1,2}$, $\lambda_{2,1}$) can be neglected. In this paper, the hydrodynamic coefficients $\mu_{j,k}$, $\lambda_{j,k}$, and f_k are computed analytically using the approach of Olaya et al. [20]. Finally, Liang et al. [21] have assumed a linear damping force F_d. Here, a nonlinear damping force of the form

$$F_\mathrm{d} = F_\mathrm{el} + F_\mathrm{mech} \tag{6}$$

is considered, where F_el is the damping force resulting from energy harvesting and

$$F_\mathrm{mech} = d_1(\dot{\xi}_2 - \dot{\xi}_1) + d_2|\dot{\xi}_2 - \dot{\xi}_1|(\dot{\xi}_2 - \dot{\xi}_1) + d_3(\dot{\xi}_2 - \dot{\xi}_1)^3 \tag{7}$$

is the velocity dependent damping force due to friction. Thereby, the coefficients d_1, d_2, and d_3 are determined by means of free decay tests. Therefore, Eq. (4) gets nonlinear, if the damping from Eqs. (6) and (7) is used. Details concerning the computation of F_el are be described in section 3.

In the simulation, a cylindrical rod with constant diameter is used, such that the hydrodynamic coefficients $\mu_{j,k}$, $\lambda_{j,k}$, and f_k can be computed analytically (see Appendix 2). However, in the experimental setup, the geometry has a slightly different shape close to the connection between rod and buoy, c.f. Fig. 2. This difference is accounted for by using additional parameters $\lambda_{\mathrm{exp},k}$ in the simulation, which can in general only be computed by matching the response of the system with experimental results. Moreover, these parameters include the viscous damping coefficients, which represent the force due to viscous drag. These coefficients are considered and experimentally computed for example by Beatty et al. [17].

2.3. Computation of the Starting Position

In order to simulate the system behavior for different geometric and mass configurations, it has to be ensured that the immersion depths of the buoy b and the plate e_1 are chosen correspondingly. Therefore, the balance of forces in z-direction is considered once again. Defining d as the thickness of the plate and ℓ as the distance between the buoy and plate for a relaxed spring, the spring force in the absence of water waves, F_0, is given by $F_0 = \kappa_\mathrm{s}(\ell-(e_1-b))$.

Inserting this in Eq. (5) leads to

$$\begin{bmatrix} \rho\pi g(R_\mathrm{b}^2 - R_\mathrm{c}^2) + \kappa_\mathrm{s} & -\kappa_\mathrm{s} \\ -\kappa_\mathrm{s} & \rho\pi g R_\mathrm{c}^2 + \kappa_\mathrm{s} \end{bmatrix} \begin{pmatrix} b \\ e_1 \end{pmatrix} = \begin{pmatrix} m_1 g - \kappa_\mathrm{s}\ell \\ m_2 g + \kappa_\mathrm{s}\ell - \rho\pi g R_\mathrm{p}^2 d \end{pmatrix}. \quad (8)$$

In each simulation, the conditions $b > 0$, $e_1 > 0$, and $e_1 > b$ have to be ensured.

2.4. Modeling of Irregular Seas

In order to simulate a realistic sea surface, a superposition of many harmonic waves is used. For this, waves with frequencies ω, corresponding wave numbers $k_\mathrm{e}(\omega)$ and amplitudes A are superposed, whereby the amplitudes are obtained from the corresponding one-sided spectral density $S(\omega)$, cf. [39, 40]. Common sea spectral densities $S(\omega)$ are the Pierson-Moskowitz spectrum for deep water and the Joint North Sea Wave Project (JONSWAP) spectrum for shallow water waves. Given a sea spectrum $S(\omega)$, the irregular long-crested sea surface can be determined by

$$Z(x,t) = \sum_{n=1}^{N_\mathrm{comp}} \cos(\omega_n t - k_\mathrm{e}(\omega_n)x + \varepsilon(\omega_n))\sqrt{2S(\omega_n)\Delta\omega_n}, \quad (9)$$

whereby the spectrum is discretized in N_comp parts with respective widths $\Delta\omega_n$ and frequencies $\omega_n \in [\omega_\mathrm{min}, \omega_\mathrm{max}]$, which do not need to be equidistant. Furthermore, $\varepsilon(\omega_n)$ is a phase shift, which is randomly distributed in the interval $[0, 2\pi]$. In the following, results for the Pierson-Moskowitz and JONSWAP spectrum will be used, which can both be described by the peak frequency ω_P and the significant wave height H_s. If not explicitly mentioned, in all further calculations the peak frequency $\omega_\mathrm{P} = 1\,\mathrm{rad/s}$ and significant wave height $H_\mathrm{s} = 2\,\mathrm{m}$ are selected.

2.5. Simulation of the Response of Random Waves

The motion of the buoy and the plate, which are excited by a harmonic wave on frequency ω, can be described by solving Eq. (4). In contrast to this, an irregular sea is described by a sum of harmonic waves, cf. Eq. (9). Therefore the question arises of how to compute the response of the system in irregular seas.

In this work, we compute the motion in irregular seas using a constant average value for all $\mu_{j,k}$ and $\lambda_{j,k}$. For a given sea spectrum, $\mu_{j,k}$ and $\lambda_{j,k}$ are

determined at $\omega = \omega_\mathrm{P}$, such that the response for waves with peak frequency ω_P is accurate. Using

$$\bar{\mu}_{j,k} := \mu_{j,k}(\omega_\mathrm{P}), \quad \bar{\lambda}_{j,k} := \lambda_{j,k}(\omega_\mathrm{P}) \quad \text{for } j,k \in \{1,2\}, \tag{10}$$

the equations of motions for irregular seas given by Eq. (9) can be stated as

$$\begin{bmatrix} m_1 + \bar{\mu}_{1,1} & \bar{\mu}_{2,1} \\ \bar{\mu}_{1,2} & m_2 + \bar{\mu}_{2,2} \end{bmatrix} \begin{pmatrix} \ddot{\xi}_1 \\ \ddot{\xi}_2 \end{pmatrix} + \begin{bmatrix} \bar{\lambda}_{1,1} + \lambda_{\mathrm{exp},1} & \bar{\lambda}_{2,1} \\ \bar{\lambda}_{1,2} & \bar{\lambda}_{2,2} + \lambda_{\mathrm{exp},2} \end{bmatrix} \begin{pmatrix} \dot{\xi}_1 \\ \dot{\xi}_2 \end{pmatrix} - \begin{pmatrix} F_\mathrm{d} \\ -F_\mathrm{d} \end{pmatrix}$$
$$+ \begin{bmatrix} \rho\pi g(R_\mathrm{b}^2 - R_\mathrm{c}^2) + \kappa_\mathrm{s} & -\kappa_\mathrm{s} \\ -\kappa_\mathrm{s} & \rho\pi g R_\mathrm{c}^2 + \kappa_\mathrm{s} \end{bmatrix} \begin{pmatrix} \xi_1 \\ \xi_2 \end{pmatrix} = \sum_{n=1}^{N_\mathrm{comp}} \mathrm{Re}\left\{ \begin{bmatrix} A_n(\omega_n) f_1(\omega_n) \mathrm{e}^{-\mathrm{i}\omega_n t} \\ A_n(\omega_n) f_2(\omega_n) \mathrm{e}^{-\mathrm{i}\omega_n t} \end{bmatrix} \right\}. \tag{11}$$

Here, N_comp is the number of harmonic components in the irregular sea; ω_n is the wave frequency of the n-th harmonic component with corresponding wave amplitude $A_n(\omega_n) = \sqrt{2S(\omega_n)\mathrm{d}\omega}\mathrm{e}^{\mathrm{i}k_\mathrm{e}(\omega_n)x + \mathrm{i}\varepsilon(\omega_n)}$, wave number $k_\mathrm{e}(\omega_n)$ and phase shift $\varepsilon(\omega_n)$ obtained from Eq. (9); the parameters $\bar{\mu}_{j,k}$, $\bar{\lambda}_{j,k}$, $f_1(\omega_n)$ and $f_2(\omega_n)$ are computed for the position of the mechanical system in still water. Thereby, it is assumed that the mechanical system is moving around the position in still water, such that the mean values of the mentioned parameters are given by their values for the position in still water. In the following, the system is assumed to be placed at $x = 0\,\mathrm{m}$. In the next section, the simulations are compared to experimental results.

2.6. Validation of Mechanical System Behavior

Before the energy output of the simulations can be investigated, the behavior of the mechanical system has to be validated first. In the following the system is considered without the generators electrical damping force F_el from Eq. (6).

In order to validate the mechanical model, an experimental setup has been constructed, where the motions of the mechanical system corresponding to different water waves can be measured. The experimental setup is shown in Fig. 3a. The dimensions given in Tab. 1 are chosen to be comparable to established drifter designs stated in section 1.2 and to fit the measurement electronics at the same time.

The facility used to undertake the experiments is the wave flume of the Institute of Mechanics and Ocean Engineering at Hamburg University of Technology. Details of the wave flume are given in Tab. 2. The waves are

Table 1: Parameter values of experimental setup.

R_b [m]	R_p [m]	R_c [m]	m_1 [kg]	m_2 [kg]	d [m]	ℓ [m]	k_f [N/m]
0.1275	0.149	0.0195	1.446	1.962	0.005	0.291	209

generated by a wave flap by a back and forth motion up to a flap angle α. The type of movement of the flap generates different water waves, such as harmonic and random waves. At the end of the wave flume a beach is installed in order to reduce the reflection of water waves. A sketch of this wave flume is shown in Fig. 3b. In all upcoming experimental results, a water depth of $h = 1.06\,\mathrm{m}$ has been used and the experimental setup is placed 6 m away from the wave flap. Since Eqs. (4) and (11) only consider vertical motions, the experimental setup is vertically guided by two rods, as shown in Fig. 3a.

Table 2: Parameter values of wave flume.

Length [m]	Width [m]	Depth [m]	Maximum wave height [m]	Maximum wave frequency [Hz]
12	1.50	1.50	0.6	2

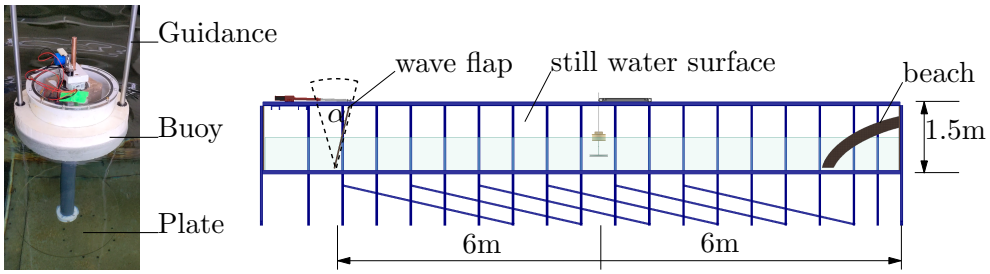

(a) (b)

Figure 3: a: Key components of the two-component wave energy converter and the guidance; b: Sketch of wave flume at the Institute of Mechanics and Ocean Engineering at Hamburg University of Technology.

The guidance leads to additional damping at the buoy, induced by mechanical friction. Together with the mechanical damping resulting from the friction between the two bodies, the corresponding damping coefficients are determined by free decay tests. Using a nonlinear ansatz, the summed damp-

ing force is assumed to be of the form

$$\mathbf{F}_{\text{damp}} = \begin{pmatrix} F_{\text{d}} + F_{\text{guidance}} \\ -F_{\text{d}} \end{pmatrix}, \tag{12}$$

whereby F_{d} is given by Eqs. (6) and (7) and F_{guidance} is assumed to be of the form

$$F_{\text{guidance}} = -d_{1,\text{g}}\dot{\xi}_1 - d_{2,\text{g}}|\dot{\xi}_1|\dot{\xi}_1 - d_{3,\text{g}}\dot{\xi}_1^{\,3}. \tag{13}$$

Therefore, the damping force in the equations of motion (4) and (11) has to be extended by the damping force of the guidance, F_{guidance}. The corresponding damping coefficients from Eqs. (7) and (13), which were determined by free decay tests, are given in Tab. 3.

Table 3: Damping parameters of experimental setup.

$d_1 \left[\frac{\text{kg}}{\text{s}}\right]$	$d_2 \left[\frac{\text{kg}}{\text{m}}\right]$	$d_3 \left[\frac{\text{kg}\cdot\text{s}}{\text{m}^2}\right]$	$d_{1,\text{g}} \left[\frac{\text{kg}}{\text{s}}\right]$	$d_{2,\text{g}} \left[\frac{\text{kg}}{\text{m}}\right]$	$d_{3,\text{g}} \left[\frac{\text{kg}\cdot\text{s}}{\text{m}^2}\right]$
36.2180	−289.6304	590.8650	7.4556	−17.7224	11.9825

Finally, the experimental correction parameters $\lambda_{\text{exp},1}$ and $\lambda_{\text{exp},2}$ have to be determined. In order to compute them, water waves of a prescribed wave frequency were generated in the wave flume and corresponding simulation data were fitted to the measured relative motion of buoy and plate. Thereby it has to be noted that even if the waves generated by the wave flap are harmonic, the length of the wave flume is finite and the beach can not absorb all incoming water waves. Therefore, reflections disturb the harmonic structure of the waves. In the simulation, this is taken into account by separating the measured water signal into its harmonic components using a Fourier series expansion and solving Eq. (11).

Figure 4 shows the measured water surface and relative motion together with the resulting simulated relative motion of the buoy and the plate after a settling time of 20 s. A capacitive sensor measures the water surface in the wave flume, while a position sensor based on a potentiometer measures relative motion. Thereby, a flap angle of $\alpha = 35°$ and an excitation frequency of $f = 0.45$ Hz have been used. For the simulation, the correction values

$$\lambda_{\text{exp},1} = 110.9337 \text{ kg/s}, \quad \lambda_{\text{exp},2} = 8.5299 \text{ kg/s} \tag{14}$$

have been considered. As can be seen, for these values the simulation data approximate the experimental data very well.

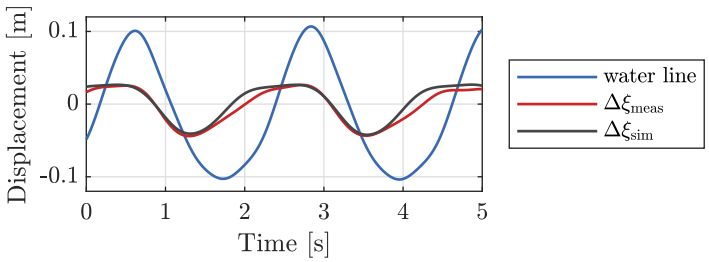

Figure 4: Comparison of experimental (ξ_{meas}) and simulation data (ξ_{sim}) for a flap angle of $\alpha = 35°$ and an excitation frequency of $f = 0.45$ Hz.

To determine whether the simulation with the stated values of $\lambda_{\text{exp},1}$ and $\lambda_{\text{exp},2}$ matches the experiment for other waves, different flap angles and wave frequencies are considered. Because of the reflection of the water waves in the wave flume, the amplitude of the waves is strongly depends on the flap angle α and wave frequency f. This can be seen in Fig. 5, which depicts the measured wave amplitude for different flap angles α and frequencies f.

The corresponding simulated and measured maximal amplitude of the relative motion is compared in Fig. 6. For frequencies lower than $f = 0.5$ Hz the simulations closely approximate the frequency-dependent relative motion measured in the experiments. For frequencies above $f = 0.5$ Hz, the difference between simulated and measured relative motion becomes larger because the relative motion in the experimental setup reaches its physical limits in contrast to the unconstrained simulation. In addition it is also possible that the buoy submerges under water, which leads to additional damping and inertial forces. These forces are not accounted for in the simulation, so it is not useful to compare simulation and experimental results for frequencies higher than $f = 0.5$ Hz. In any case, seawater waves are unlikely to excite the buoy at such high frequencies. As a result, Eqs. (4) and (11) are appropriate and validated for modeling the vertical motion of the buoy and plate.

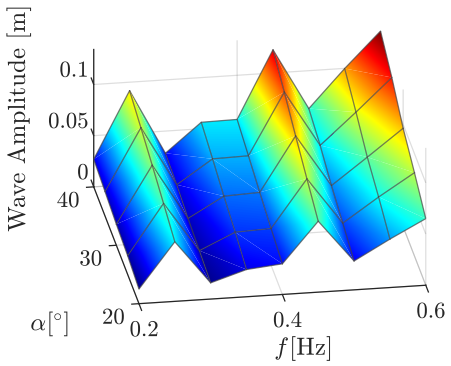

Figure 5: Amplitude of measured water waves for different flap angles α and frequencies f.

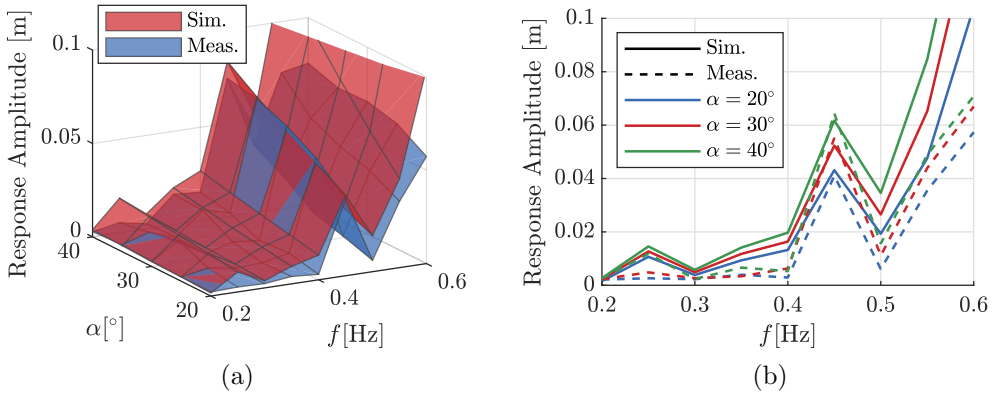

Figure 6: Simulated (sim.) and measured (meas.) maximum amplitude of relative motion between buoy and plate for different flap angles α and wave frequencies f shown in two plots. a: 3D plot of the response amplitude of all evaluated flap angles and wave frequencies. b: Corresponding 2D plot of the response amplitude for $\alpha \in \{20°, 30°, 40°\}$.

3. Design of Electromagnetic Power Take-off

For the conversion of the relative motion into electrical energy, a generator is designed in the following. The requirements for the generator are determined from the dynamic analysis in the previous chapter and a parametrisation of the selected generator concept is carried out. Finally, an implementation is tested on a testbench and used for simulation model validation.

3.1. Generator Requirements

It is assumed that realistic seawater waves have the highest probability to be in the range between 0.5 and 2 rad/s, which provide a relative motion between 0 and 1 m/s. The generator should have the lowest possible cogging force F_{el} in order to limit the damping force in the mechanical system. The available acting forces between buoy and plate can be estimated from the masses and accelerations of the experimental setup. In order to allow dynamic system responses, F_{el} should be kept below 10 N. The output voltage of the generator must be high enough to allow current rectification and the power output must be maximised, with a minimum power target of 10 mW (section 1.2).

3.2. Generator Working Principle

The fundamental functionality of an FSPMLM described in several publications [27, 32, 41] consists of the translator and the stator armature (Fig. 7a). The passive translator has a regular arrangement of translator poles with con-

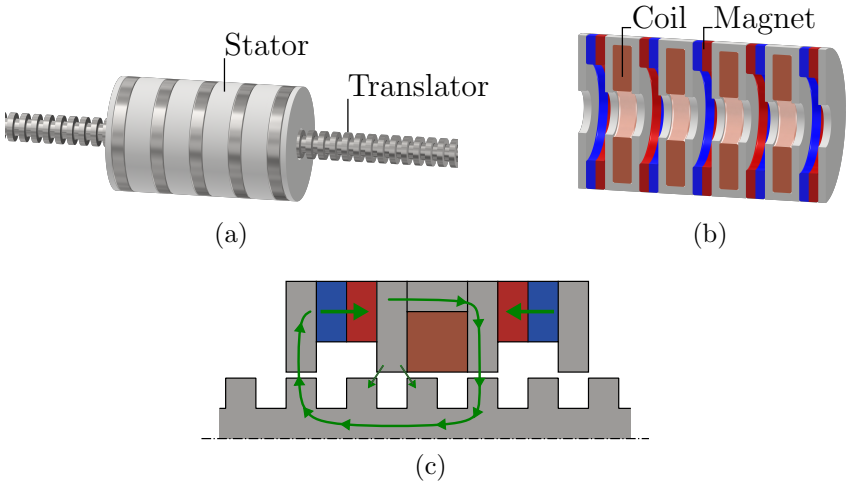

Figure 7: a: 3D representation of FSPMLM consists of the components stator and translator; b: Implementation of the stator with visualisation of magnets and coils; c: FSPMLM concept with translator plurality, magnetic flux indicated by green arrows.

stant pole pitch, the stator consists of stator slots with alternating coils and magnets (Fig. 7b). Starting from the position shown in Fig. 7c, movement by half a pole pitch results in a change of flux direction through the coil due to the opposite magnetic orientation. After a complete movement of

the translator by the distance of the pole pitch τ_p, the flux direction returns to the initial state, which describes a full generator period. A continuous movement leads to a continuous flux linkage and thus to the induction of an electromagnetic force (EMF) in the coil. The frequency of flux switching is determined by the speed of the translator and the pole pitch. The selected FSPMLM design, shown in Fig. 7c, has a plurality of translator poles and therefore has a slot/pole ratio of 2/3. Compared to other designs [33, 41, 42], a plurality of poles enables fast flux switching even at low amplitudes and speeds. This feature is particularly useful for wave energy conversion and can be seen in several existing implementations [31, 43].

Large-scale flux switching machines are designed for three-phase sinusoidal EMF by choosing a multiple of three for the number of coils and adjusting the translator spacing to implement a 120° phase shift between coils [32, 43]. For this small energy harvesting application, the AC output voltage of each coil is rectified to DC to charge the Drifter's power supply. Therefore, a three-phase voltage is not essential, so the number of coils and the resulting tooth pitch can be chosen to fit into the Drifters dimensions.

3.3. Generator Design

In order to keep manufacturing costs low, the assembly consists of parts easy to manufacture. Only rings, discs and inexpensive off the-shelf magnets are used for the overall construction of the stator. The rectangular shape of the poles simplifies the machining of the translator. Previous publications [44] have shown how the magnetic flux can be optimized in the design, which is neglected here to avoid much higher machining effort and cost. This work focuses on a low-cost design and therefore omits the flux optimization and investigates what performance can still be achieved.

The dimensioning of the generator is done in three steps. First, the design of the stator is mainly determined by the availability of the components and the requirements for the external dimensions. Then the influence of the pole pitch of the translator is investigated. Finally, the shape of the translator pole is adapted to the chosen pole pitch.

The most important evaluation criterion for the overall design is the conversion efficiency of the generator. The design aims to maximise the electromagnetic conversion and minimise the cogging forces F_{el} to allow high response amplitudes for the dynamic system.

3.3.1. Stator Optimization

Fig. 8 shows one stator segment with its coil and two opposed magnets. At the beginning the magnet dimension is selected, because many stator parameters depend on it. In order to keep the cost of the magnets low, standard dimensions are used. One of the largest standard neodymium ring magnets found has an outer diameter of 40 mm, inner diameter of 25 mm, height of 5 mm and a unit price of less than 5 €. The inner radius of the stator is chosen to allow for a structurally stable translator while providing enough space for the coil windings. A plurality of translator poles requires a uniform stator slot pitch τ_s, which implies that the magnet width W_M and the coil width W_C must have the same length. In order to allow high induction voltage, the number of coil turns should be increased. Using a 0.1 mm coil wire, the installation space of one coil allows 3000 turns. With the determined parameters, up to four stator segments in a row can be arranged in the Drifter. The resulting stator design is shown in Fig. 8 and the dimensions can be seen in Tab. 4.

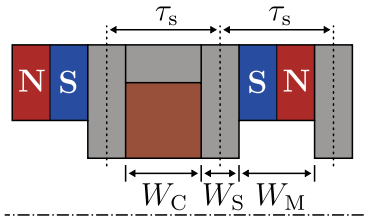

Figure 8: Visualisation of the stator parameter slot pitch τ_s, coil width W_C, magnet width W_M and tooth width W_S.

Table 4: Stator dimensions of the designed linear generator.

Outer radius of stator	Inner radius of stator	Outer radius of translator	W_M	W_C	W_S	τ_s	No. of coils
20mm	5.5mm	5mm	5mm	5mm	2mm	7mm	4

3.3.2. Translator Pole Pitch Optimization

For the given stator design, the translator must be parameterised to minimise cogging forces and maximise power output. Based on the rectangular translator poles shown in Fig. 9, three design parameters can be adjusted: pole pitch τ_p, pole width W_T and pole height H_T. In this section we examine

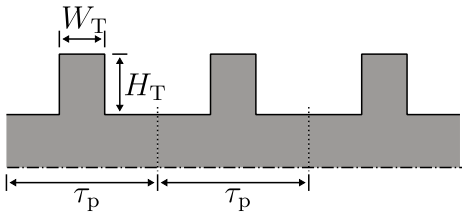

Figure 9: Visualisation of the translator parameter pole width W_T, pole height H_T and pole pitch τ_p.

the influence of pole pitch τ_p and in the following section we examine pole dimensions by its width W_T and height H_T.
The pole pitch is determined by the slot/pole ratio, which is chosen close to 3/2 (Fig. 7c) to ensure a plurality of poles. With an exact ratio of 3/2, the flux linkage of all four stator segments is synchronised and the force peaks of the individual sections would add up and lead to undesirably high total cogging forces. In order to achieve a uniform distribution of EMF and force peaks, a relative pole shift δ can be added to the slot/pole ratio:

$$\tau_\mathrm{p} = \tau_\mathrm{s} \cdot \frac{2}{3 \pm \delta} \tag{15}$$

For a uniform EMF distribution the pole shift has to be adapted to the number of stator sections N_s, such that

$$\delta = \frac{1}{N_\mathrm{s}} \Rightarrow \tau_\mathrm{p} = \tau_\mathrm{s} \cdot \frac{2}{3 \pm \frac{1}{N_\mathrm{s}}} \tag{16}$$

The phase shift between the coils for the EMF induction is then given by

$$\phi = 360° \cdot \delta = \frac{360°}{N_\mathrm{s}} \tag{17}$$

A three phase generator with a coil number $N_\mathrm{s} = 3$, results in a phase shift of 120°. For the four coil system ($N_\mathrm{s} = 4$) considered here, a uniform EMF distribution over all coils leads to a phase shift $\phi = 90°$. If N_s is an even number, the pole shift can be selected to multiples of δ. The shift $2\delta = \frac{1}{2}$ for a four coil system would distribute the EMF over the first and second coil uniformly and synchronize linkage of the first and the third, as well as second and the fourth coil. With a counter-pole arrangement of the magnets, this leads to an in-phase induction in all coils simultaneously.

For the here considered four coil setup, four possible pole pitch configurations with uniform EMF and cogging force can be calculated. With a slot pitch of $\tau_s = 7\,\text{mm}$, the possible pole pitches τ_p are given in Tab. 5.

Table 5: Possible pole pitch configurations with uniform EMF distribution.

$\tau_s \frac{2}{3+\frac{1}{2}}$	$\tau_s \frac{2}{3+\frac{1}{4}}$	$\tau_s \frac{2}{3-\frac{1}{4}}$	$\tau_s \frac{2}{3-\frac{1}{2}}$
4 mm	4.3 mm	5.1 mm	5.6mm

A FEM analysis is performed using a cylindrical 2D model of the generator and the simulation software ANSYS electronics desktop. Fig. 10a shows a plot of the model with the resulting magnetic flux densities and Fig. 10b shows the meshing resolution applied. ANSYS transient solver is used to solve Maxwell's equations for a moving translator at constant speed.

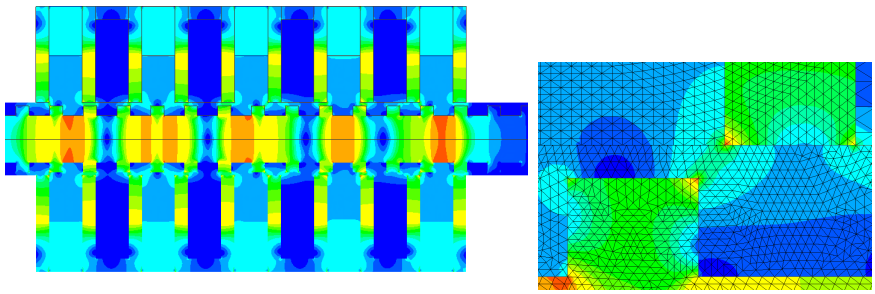

(a) (b)

Figure 10: FEM-Simulation setup shows the B-Fields of the generator in (a) and the meshing in (b).

The optimization of the pole pitch requires a joint consideration of the parameters of pole pitch τ_p and pole width W_T, since the time behavior of the flux linkage is influenced by the combination of both. For now the pole height is set to a constant value of $H_T = 1.5\,\text{mm}$ and will only be varied for the optimization of the pole dimensions in the next section.

To allow a comparison between the results of translators with different pole pitches τ_p, the simulation is carried out for one generator period and the movement is considered relative to the pole pitch. At first, the translator velocity is set to $0.1\,\text{m/s}$. An impedance-matched resistance of $500\,\Omega$ is used as the load for each coil. Fig. 11 shows the results of the simulated parameter variation for τ_p and W_T. No solution exists for combinations in which $W_T >=$

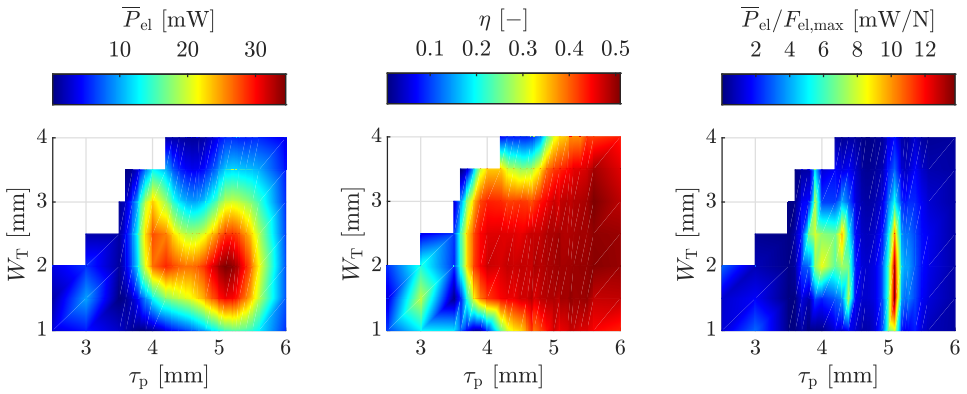

Figure 11: Simulation results of the parametric simulation over the pole pitch τ_{p} and pole width W_{T} for the a: Electrical power b: Efficiency c: Ratio of power to max. cogging force

τ_{p}, since the pole width always has to be smaller than the pole pitch. In Fig. 11a the average electrical Power $\overline{P}_{\mathrm{el}}$ as the sum of all coils is displayed:

$$\overline{P}_{\mathrm{el}} = \frac{1}{t_{\mathrm{p}}} \int_0^{t_{\mathrm{p}}} \sum_{i=1}^{4} V_i \cdot I_i \, \mathrm{d}t, \tag{18}$$

V_i and I_i represent the voltage and current of the coil i and t_{p} is the required time for the translator movement by one pole pitch τ_{p}. It can be seen that the average electrical power has maximum values for a pole pitch around 4 and 5 mm and a pole width close to the stator tooth width of $W_{\mathrm{S}} = 2\,\mathrm{mm}$. The average mechanical power $\overline{P}_{\mathrm{mech}}$ is calculated by the product of cogging force F_{el} and velocity v. The efficiency η shown in Fig. 11b as the ratio of $\overline{P}_{\mathrm{el}}$ to $\overline{P}_{\mathrm{mech}}$:

$$\overline{P}_{\mathrm{mech}} = \frac{1}{t_{\mathrm{p}}} \int_0^{t_{\mathrm{p}}} F_{\mathrm{el}} \cdot v \, \mathrm{d}t \quad \text{and} \quad \eta = \frac{\overline{P}_{\mathrm{el}}}{\overline{P}_{\mathrm{mech}}} \tag{19}$$

It is shown that η increases to a plateau for pole pitches greater than $\tau_{\mathrm{p}} = 3.8\,\mathrm{mm}$.

In order to allow a simultaneous consideration of the force and power, the ratio of the average electrical power to the maximum force is shown in

Fig. 11c. $F_{\mathrm{el,max}}$ is given by the maximum force peak in one pole pitch period:

$$F_{\mathrm{el,max}} = \max_{t\in[0,t_{\mathrm{p}}]} F_{\mathrm{el}}(t). \tag{20}$$

It is noticeable that the calculated pole pitches in Tab. 5 show good results in Fig. 11c. In particular, the pole pitch of $\tau_{\mathrm{p}} = 5.1\,\mathrm{mm}$ has a high ratio for a wide range of tooth width, but shows strong degradations with only small deviations from the pitch value. Between $\tau_{\mathrm{p}} = 4.0\,\mathrm{mm}$ and $4.3\,\mathrm{mm}$ a whole range of pitches shows good results, but in a narrower band for the pole width. Only the pitch of $\tau_{\mathrm{p}} = 5.6\,\mathrm{mm}$ is not represented with good results in Fig. 11c. Due to the slot pole ratio 2/2.5, the pole spacing τ_{p} becomes too large to implement the principles of a flux switching machine.

Fig. 12 shows the corresponding flux linkage of the coils over time. The EMF in all four coils are synchronised for $\tau_{\mathrm{p}} = 4\,\mathrm{mm}$. The phase shift for $\tau_{\mathrm{p}} = 4.3\,\mathrm{mm}$ and $5.1\,\mathrm{mm}$ evenly distributes the flux linkage as expected. In a generator design that produces a very small output voltage, the synchronised coupling of $\tau_{\mathrm{p}} = 4\,\mathrm{mm}$ could be used to connect all the coils in series to increase the total output voltage. In any other design, an even distribution of flux linkage is advantageous to ensure a uniform charging current on the DC side.

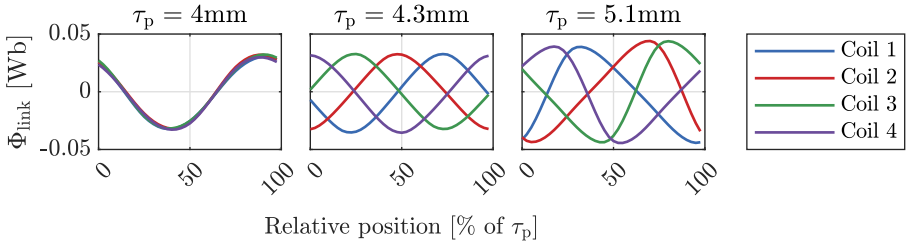

Figure 12: Flux linkage of all four coils for different translator dimensions.

3.3.3. Translator Pole Dimension Optimization

In order to analyze the influence of the pole shape by the width W_{T} and height H_{T} displayed in Fig. 9, a parametric simulation is performed for the pitches $\tau_{\mathrm{p}} = 4\,\mathrm{mm}, 4.3\,\mathrm{mm}$ and $5.1\,\mathrm{mm}$. Fig. 13 shows the results for the three translator pitches over the entire parameter range in a 3D plot and for a constant value of W_{T} over the parameter of H_{T}. It can be seen that the electrical power is similar for all three pole pitch variants.

The biggest difference occurs in the value of the maximum cogging force. The translators with $\tau_\mathrm{p} = 4\,\mathrm{mm}$ and $4.3\,\mathrm{mm}$ show large cogging forces over the majority of the parameter range with the exception of a narrow local minimum. The translator with $5.1\,\mathrm{mm}$ on the other hand shows a low cogging force for almost the entire considered range. It is likely that for the first two translators a very specific local minimum has been found, which can exist in an ideal implementation, but is difficult to reproduce in an actual implementation. The pole pitch of $\tau_\mathrm{p} = 5.1\,\mathrm{mm}$ might be less prone to manufacturing inaccuracies.

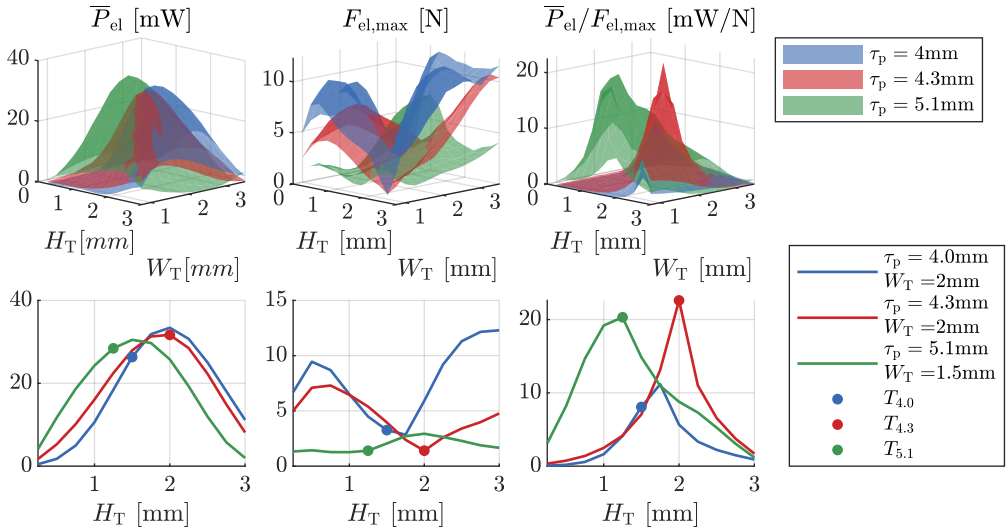

Figure 13: Simulation results of the parametric simulation over pole width W_T and pole height H_T in a 3D-plot (top) and for a constant value of W_T over H_T (bottom). The implemented translator dimensions $T_{4.0}$, $T_{4.3}$ and $T_{5.1}$ are marked in the lower plots.

3.4. Linear Generator Testing

In the following, the linear generator is implemented to validate the FEM results and to test the design using the test bench shown in Fig. 14. Based on the parametric analyzes performed, the dimensions of the translator shown in Tab. 6 are selected for implementation. The chosen dimensions have low values for the cogging force and at the same time have a good ratio between electrical power and force (cf. Fig. 13).

The testbench is implemented using a LinMot linear motor, a force sensor and an implementation of the FSPMLM designed above. The excitation

Table 6: Implemented translator dimensions.

	$T_{4.0}$	$T_{4.3}$	$T_{5.1}$
τ_p	4.0 mm	4.3 mm	5.1 mm
H_T	1.5 mm	2.0 mm	1.25 mm
W_T	2.0 mm	2.0 mm	1.5 mm

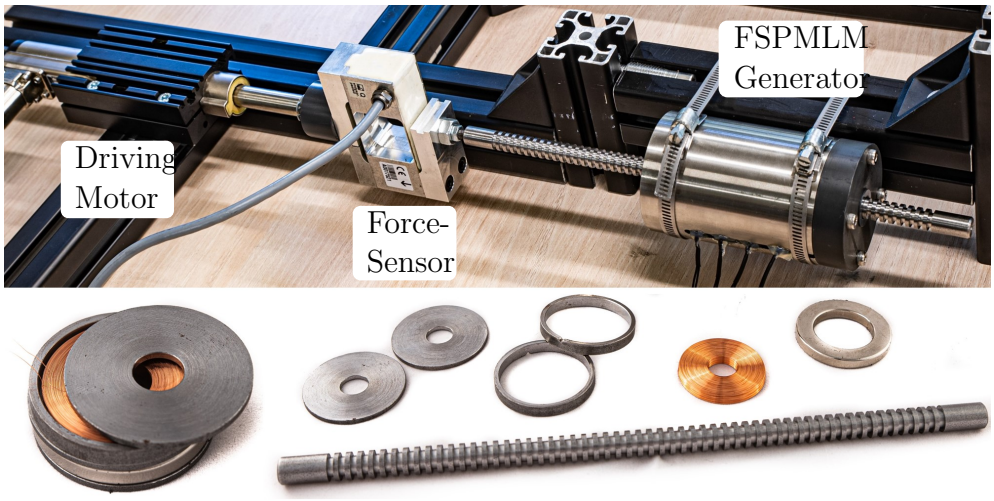

Figure 14: Testbench for the implemented generator (top) and the assembly parts of the linear generator (bottom).

and data processing is controlled by a connected PLC, which allows arbitrary movements and the measurement of current and voltage. The designed FSPMLM is made of inexpensive mild steel and the stator has the dimensions described in Tab. 4. Fig. 14 shows the assembly of a magnet and a coil on the bottom left and the individual components are shown side by side on the right.

Three translator implementations (Tab. 6) are tested for a target speed of 0.1 m/s. Due to the cogging forces of the generator and the constraints of the testbench control loop, the actual speed of the translator is not perfectly constant. In order to represent the actual motion profile of the measurement in the simulation, the FEM analysis is carried out for a range of constant speeds and fitted to the actual speed of the translator by a linear interpolation. A comparison between the measurement and the linear interpolated FEM results is shown in Fig. 15. The results are presented over the relative

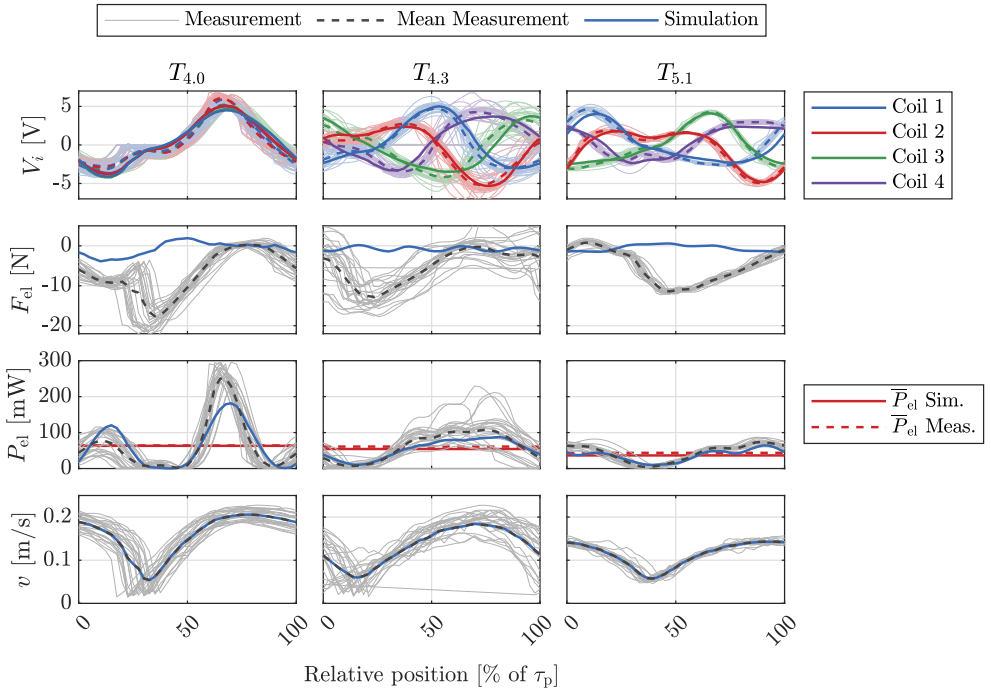

Figure 15: Comparison between measurement and simulation data for the movement of one generator period with three different translator dimensions. Shown curves are voltage output of single coil V_i, total electrical power over time P_{el}, mean power $\overline{P}_{\mathrm{el}}$, cogging force F_{el} and translator velocity v.

position of the translator with respect to the pole pitch. The continuous measurement series is divided into sections of equal length by taking the modulo of the absolute position through the pole pitch. The average of the series of measurements is represented by the dashed line. It can be seen that the voltage curves of the simulation and the average measurement show very good agreement in amplitude and phase for all three translator dimensions. Same applies to the output power, especially when considering the mean power $\overline{P}_{\mathrm{el}}$ which has similar values for all three translator dimensions. Over time, the value of P_{el} strongly varies between the tree translator types. The synchronous flux for the translator $T_{4.0}$ results in large fluctuations in the output power. On the other hand, $T_{5.1}$ has a very uniform power distribution over time.

The smallest cogging force peaks in the measurement results can be observed with $T_{5.1}$. For all translators, the force measurement is significantly

larger compared to the FEM results, whereas $T_{5.1}$ shows the smallest offset. It is suspected that the local optima for $T_{4.0}$ and $T_{4.3}$ were in fact not exactly met, while the low cogging force of translator $T_{5.1}$ can be achieved even with the applied manufacturing tolerances. But even $T_{5.1}$ shows a large difference between the simulated and the measured cogging force. As a second effect, it is assumed that a radial offset of the translator to the stator contributes to the mismatch. The radial offset leads to strong radial forces which act on the installed bearings and lead to strong friction and thus to an increase in the axial forces. This suspicion is confirmed by a test with a translator of the same material with no poles and constant diameter. The movement of the rod should require only a small effort due to the missing air gaps but was measured to a constant force of $> 20\,\mathrm{N}$. A translator rod made from non-magnetic aluminium shows a lower constant friction force of $3\,\mathrm{N}$. Despite high accuracy requirements, such radial mismatch is difficult to avoid. This has a particularly high impact on translators with a small air gap, as more magnetic material is available for axial forces. To reduce friction forces in future applications, greater attention must be paid to the cylindrical coaxiality tolerance. In addition, the force transmission of the connecting rod on the translator must be well aligned, or a joint between the connecting rod and translator can be used to reduce the transmission of radial forces. The influences on the dynamic behavior have to be investigated in this respect. From the available measurements, it appears that $T_{5.1}$ offers the best ratio between power and cogging force and is therefore selected for the design of the generator.

3.5. Design Performance and Model Correction

In order to further analyze the performance of the selected design with the translator $T_{5.1}$, the generator is tested with a range of different translator speeds. A series of FEM simulations allows a comparison with the measurement results. It can be seen in Fig. 16 that simulation and measurement show good agreement over the entire velocity range from 0.02 to $0.6\,\mathrm{m/s}$. Thereby, $V_{\mathrm{RMS},i}$ represents the root mean square of the voltage for a single coil and $\overline{P}_{\mathrm{el}}$ describes the mean power for the sum of all four coils. Due to the large number of coil turns, the voltage output has a sufficient level even at low translator speeds. The minimum target power of $10\,\mathrm{mW}$ requires a translator speed of $0.05\,\mathrm{m/s}$. At $0.2\,\mathrm{m/s}$ the power is about $100\,\mathrm{mW}$ and has a voltage level of $3\,\mathrm{V}$. Higher translator speeds bring a significant increase

in power. It should be noted that the movement is not uniform due to the cogging of the translator and therefore speed and power peaks occur.

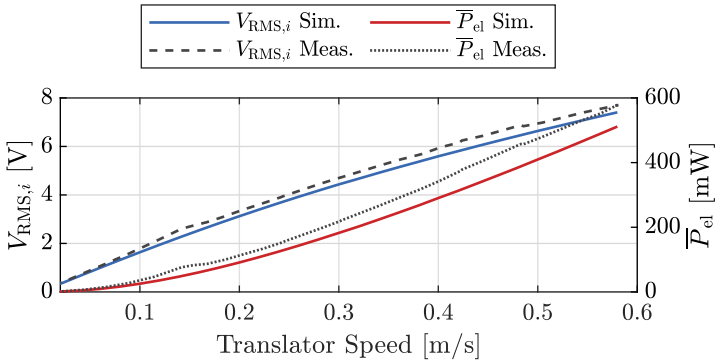

Figure 16: Comparison between measurement data and simulation for the translator $T_{5.1}$. Shown curves are the rms voltage of a single coil $V_{\mathrm{RMS},i}$ and the mean electrical power $\overline{P}_{\mathrm{el}}$.

The FEM model gives a good position and velocity dependent simulative estimation of the power output. Only the generator forces of the FEM simulation do not coincide with the measurement results (Fig. 17). Further modeling of the entire system uses interpolated measurement data to allow the simulative coupling of the actual generator implementation with the mechanical model. Fig. 17 shows a comparison of the interpolation data for the measured forces F_{M} and the simulated forces F_{S}, which can be used for the generator damping force F_{el} in the equations of motion in Eq. 6.

4. Model Coupling and Optimization

So far, the mechanical model of the WEC and the electromagnetic model of the generator have been considered separately. In this section, the coupled system is analyzed for the first time to allow an estimation of the expected power output.

4.1. Model Coupling

For the coupling of the two systems, the developed equations of motion of the dynamic model are joined with the generator damping force F_{el}. The power output of the generator is calculated based on the WEC motion and a FEM-Model data interpolation. Fig. 18 shows the excitation of the coupled

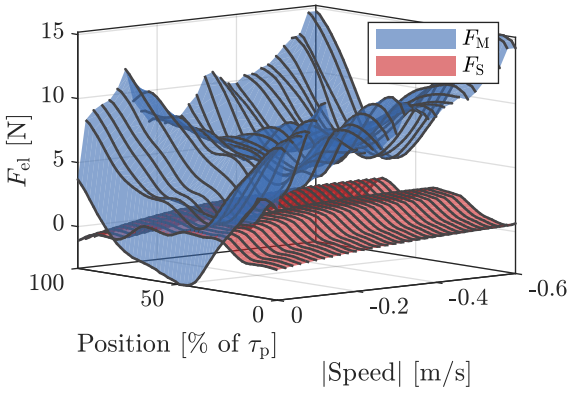

Figure 17: Comparison between the measured cogging Force F_M and the simulated cogging Force F_S of translator $T_{5.1}$. The red and blue surface plot represents the interpolation of the simulated or measured data points.

system with a regular wave at $\omega = 1\,\mathrm{rad/s}$ and an amplitude of 1 m. The relative motion $\xi_2 - \xi_1$ results from the motions of the buoy ξ_1 and the plate ξ_2 in relation to each other. To analyze the influence of the generator damping force on the system dynamics, Fig. 18 compares two simulation results with different generator forces. An ideal generator simulation with very low cogging forces $F_{el} = F_S$ shows a larger system response than the simulation based on the measured generator interpolation with $F_{el} = F_M$. This can also be seen in the power average P_{avg} over the considered time period, as the simulation using the higher force interpolation F_M produces a lower power average of 150 mW compared to 200 mW generated by the system using lower force interpolation F_S. To allow a realistic approximation, the generator force is implemented by the interpolation of the measured force $F_{el} = F_M$ in the following.

4.2. Optimization of System Parameters

Since the electrical power output is related to the relative velocity, the question arises how the system parameters stated in Tab. 1 can be influenced such that the response amplitude of the relative velocity between the buoy and the plate increases. Therefore, the relative velocity in irregular seas with a broadband sea spectrum is studied. Using Monte-Carlo simulations, the optimal system parameters are determined in the following way:

1. For a prescribed peak frequency $\omega_P \in [\omega_{min}, \omega_{max}]$ and significant wave

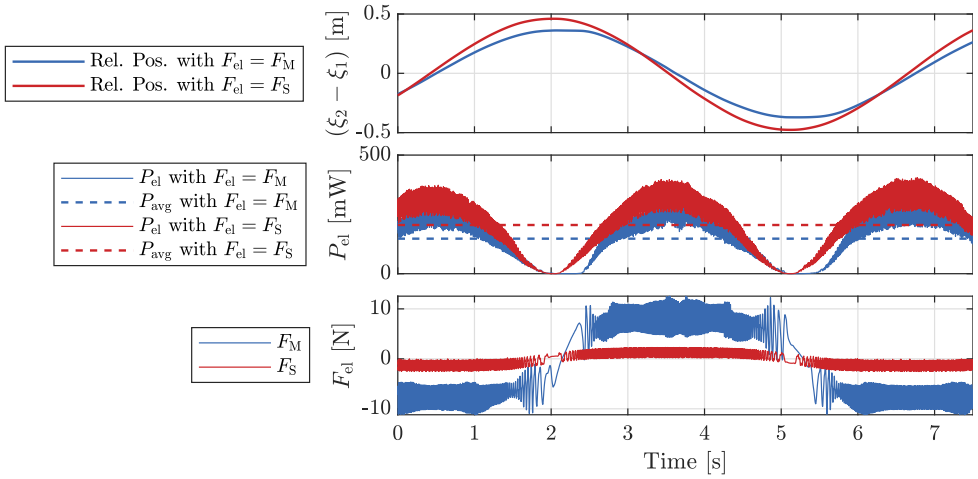

Figure 18: Simulation results of the coupled system. Relative displacement $\xi_2 - \xi_1$ (top); Electrical power output P_{el} and average over time P_{avg} (middle); Generator damping force F_{el} (bottom).

height H_s, generate an irregular seas for times $t \leq T_{end}$.

2. Compute the corresponding relative velocities by solving Eq. (11) and calculating the differences $\dot{\xi}_1 - \dot{\xi}_2$.

3. Compute the corresponding upper envelope of the relative velocity, which is a smooth curve outlining the maxima of the relative velocity.

4. Compute a histogram over the generated envelope and normalize it by the number N of all data points. Then

$$\frac{1}{N} \sum_{i=1}^{I} h_i = 1. \tag{21}$$

Thereby, h_i denotes the number of times the relative velocity has a value in the interval $[(i - 1/2)\frac{v_{max}}{I}, (i + 1/2)\frac{v_{max}}{I}]$ for $i \in \{1, \ldots, I\}$, whereby v_{max} is the maximal reached velocity and I is the number of velocity intervals.

5. Do the first four steps for $R \in \mathbb{N}$ different peak frequencies $\omega_P \in [\omega_{min}, \omega_{max}]$. Sum up all counts in the R different histograms, where the corresponding relative velocities are higher than a prescribed number Γ. This sum is denoted by G.

In point 3. of the simulation scheme, the envelope of the velocity is used because by this means the maximal velocity values are represented and can be optimized. In the following, the system parameters from Tab. 1 are optimized with respect to the objective function:

$$\text{maximize } G = \sum_{j=1}^{R} \frac{1}{N_j} \sum_{i=1}^{I_j} h_{i,j}, \quad \text{for } h_{i,j} \text{ considering only relative velocities} > \Gamma. \tag{22}$$

Thereby, $h_{i,j}$, N_j and I_j are the respective values of h_i, N and I from point 4. of the simulation scheme for the j-th peak frequency $\omega_{\mathrm{P,j}}$, $j = 1, \ldots, R$. By choosing Γ, the amount of relative velocities higher than Γ is optimized. If Γ would be set to zero, then the velocities could also be very close to zero and the optimization condition would be fulfilled, although no relative velocities would occur in the system.

It has to be ensured that the geometry of the optimized system still meets the requirements of compact Drifter dimensions. Therefore, in the optimization process the optimization parameters are restricted. For the computation of this optimization problem the interior-point method is used, see e.g. [45]. But also other gradient based optimization methods for the computation of nonlinear programming problems can be used for the described optimization problem. Tab. 7 summarizes the optimized system parameters for two different cases. In both cases, all radii are forced to be smaller than 0.5 m, distance ℓ smaller than 0.5 m, thickness of the plate smaller than 0.2 m, both masses smaller than 5 kg and the spring constant k_f smaller than 300 N/m. Moreover, the optimization is performed with respect to seas with a Pierson-Moskowitz spectrum with peak frequencies $[\omega_{\min}, \omega_{\max}] = [0.8, 1.2]$ rad/s and fixed significant wave height $H_{\mathrm{s}} = 2\,\mathrm{m}$ or $H_{\mathrm{s}} = 3\,\mathrm{m}$. Optimizations with these two values for H_{s} lead to almost the same results for the optimized system parameters, if starting from the optimized parameter values for $H_{\mathrm{s}} = 2\,\mathrm{m}$. Thereby, irregular seas with $N_{\mathrm{comp}} = 100$ harmonic components are simulated for $T_{\mathrm{end}} = 40\,000\,\mathrm{s}$. The optimization algorithm maximizes the number of counts in the histograms, where the corresponding relative velocities are higher than 0.4 m/s, i.e. $\Gamma = 0.4\,\mathrm{m/s}$. For all simulations, damping parameters summarized in Tab. 3 and Eq. (14) are used. The electrical damping force F_{el} from Eq. (6) is represented by the interpolation of the measured generator force F_{M} from section 3.

Fig. 19 compares the geometries of the resulting optimized WECs with the experimental setup, whereby still water is considered. It can be seen that

the system parameters of WEC A are more comparable with parameters of the WEC in the experiment than the parameters of WEC B, which has a small ratio of $R_\mathrm{b}/R_\mathrm{p}$ and a far higher mass m_1.

In order to compare the improved behavior of the optimized WECs and the experimental setup of the WEC, Fig. 20 shows the corresponding normalized histograms for peak frequencies $\omega_\mathrm{P} \in [0.1, 4]$ rad/s and $H_\mathrm{s} = 2\,\mathrm{m}$ for the experimental WEC setup and the optimized WECs from two different perspectives. It is illustrated that the mechanical system corresponding to the optimized parameters leads to a more broadband distribution of simulated relative velocities for given peak frequencies than the initial experimental WEC setup. Moreover, for frequencies lower than 1.5 rad/s, the optimized parameters lead to higher relative velocities. Therefore, much more energy can be harvested for a broadband sea spectrum from the WECs designed with the optimized system parameters than with the parameters of the experimental WEC. In the next section, the amount of harvested energy is studied.

Table 7: Parameter values of optimized system regarding a Pierson-Moskowitz spectrum with peak frequency $\omega_\mathrm{P} \in [0.8, 1.2]$ rad/s and significant wave heights $H_\mathrm{s} = 2\,\mathrm{m}$.

System	R_b [m]	R_p [m]	R_c [m]	m_1 [kg]	m_2 [kg]	d [m]	ℓ [m]	k_f [N/m]
A	0.120	0.250	0.01	1.188	4.351	0.017	0.418	192.07
B	0.085	0.289	0.01	4.991	4.794	0.017	0.455	127.80

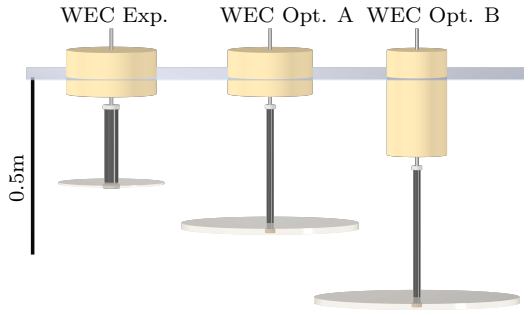

Figure 19: Comparison of the dimensions between the implemented WEC prototype from the experiments to the parameters of the optimized WECs. WEC from experiments on the left, optimized WECs on the right.

It has to be noted that the maximal velocities are not reached by the optimized WECs at frequencies around $\omega_\mathrm{P} \approx 1$ rad/s, for which the optimization

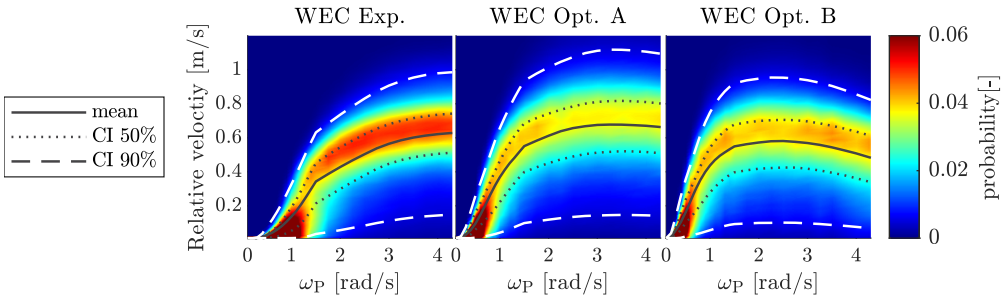

Figure 20: Probability of response amplitude of relative velocity for different peak frequencies ω_P using the Pierson-Moskowitz sea spectrum. Results for the test system with system parameters given in Tab. 1 on the left. Results for the optimized system with system parameters given in Tab. 7 shown on the right. The results are given for a significant wave height of $H_s = 2\,\mathrm{m}$.

has been performed but at frequencies around 3.5 rad/s. This is due to the fact that for $\omega_P \approx 1$ rad/s, both bodies have a large relative motion. But since they are excited by waves with small wave frequency, the relative velocity is slow. This can be optimized further if optimization parameters like the distance ℓ are allowed to be bigger than the prescribed values, which is conflicting with the compact Drifter dimensions. Moreover, it may happen in the simulations that the two bodies collide. Then, the simulation is restarted, since at the time of the collision, extra impact forces would need to be considered. The corresponding computations would need a very accurate simulation of the impact itself, since the contact time is very short and therefore the simulation of the impact needs a very short time step [46, 47]. This would make the simulation very time consuming. In addition to this, the bodies only collide for a high relative motion, which rarely occurs.

4.3. Overall Power Output

In the following, the power output of the coupled system in irregular waves is considered. In order to determine the expected value of the power output in irregular waves, a series of simulations is performed for each peak frequency ω_P. As a result, the expected average power P_{avg} along with 95% confidence intervals is shown in Fig. 21. The expected power output values for the model from the experiment and the optimized designs A and B including the coupling with the generator are compared. It is obvious that the optimized systems represent a strong improvement in output power. Looking at the wave spectra, the starting frequency for the experimental setup is relatively

high at about 1 rad/s, which means that the expected output is insufficient in typical ocean waves. For the optimized models A and B, this starting frequency is lowered to about 0.5 rad/s, which promises a significantly higher output power and enables the use in real seas. A real sea state with peak frequency $\omega_\mathrm{P} = 1\,\mathrm{rad/s}$ and significant wave height of $H_\mathrm{s} = 2\,\mathrm{m}$ leads to an expected power output of about 130 mW for system A and 180 mW for system B.

It should be noted that the performance calculated here results only from model simulations and actual implementation may yield lower performance, especially when rectification, electrical circuits and power storage are taken into account. However, the minimum performance requirements are much lower and therefore can be met with both optimized systems. With its lower mass and dimensions closer to the original system, model A is the preferred variant, but using model B as an example, it can be shown that further mechanical optimization is possible through variations in shape, weight and spring constant. In the electromagnetic domain, further optimization should consider the number of coil turns to adapt the voltage level for efficient rectification and energy storage.

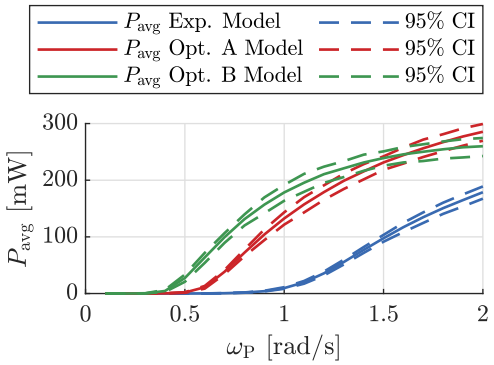

Figure 21: Simulation result comparison for the power output of the experiment system with the optimized systems A and B in random waves with different peak frequencies ω_P using the Pierson-Moskowitz sea spectrum and a significant wave height of $H_\mathrm{s} = 2\,\mathrm{m}$.

5. Conclusion

The aim of this work is to develop and optimize a wave energy converter that can be integrated into a small, free-floating sensor Drifter. Specific development criteria in terms of power, size and cost have been established. The

mechanical and electromagnetic implementation of the WEC has been investigated using experimental and simulation results. It has been found that the equations of motion and the generator model are largely consistent with the experimental results. Furthermore, the electrical modeling has enabled the design of a linear generator that meets the performance requirements of the WEC and provides sufficient voltage levels at low translator speeds. Coupling the mechanical and electrical model has allowed an optimization of the mechanical system parameters achieving a high system response even at low wave frequencies and amplitudes. Providing a simulated potential power output of 130 mW in random waves with a peak frequency of 1 rad/s and a significant wave height of $H_s = 2\,\mathrm{m}$, the developed WEC meets the requirements in terms of performance and dimensioning and can be adapted to be used in sensor Drifters. It is the first time that the proposed WEC type is designed and optimized for drifting sensor platforms. In future work, the fully coupled system will be build and tested in experiments in order to further investigate the wave energy conversion for small drifting platforms in realistic sea waves.

References

[1] G. Wu, Z. Lu, Z. Luo, J. Shang, C. Sun, Y. Zhu, Experimental analysis of a novel adaptively counter-rotating wave energy converter for powering drifters, Journal of Marine Science and Engineering 7 (6) (2019). doi:10.3390/jmse7060171.

[2] A. Babarit, Ocean wave energy conversion: resource, technologies and performance, Elsevier, 2017.

[3] R. Hine, S. Willcox, G. Hine, T. Richardson, The wave glider: A wave-powered autonomous marine vehicle, in: OCEANS 2009, 2009, pp. 1–6. doi:10.23919/OCEANS.2009.5422129.

[4] W. Ding, B. Song, Z. Mao, K. Wang, Experimental investigation on an ocean kinetic energy harvester for underwater gliders, in: 2015 IEEE Energy Conversion Congress and Exposition (ECCE), 2015, pp. 1035–1038. doi:10.1109/ECCE.2015.7309802.

[5] C. D. Haldeman, O. Schofield, D. C. Webb, T. I. Valdez, J. A. Jones, Implementation of energy harvesting system for powering thermal glid-

ers for long duration ocean research, in: OCEANS 2015 - MTS/IEEE Washington, 2015, pp. 1–5. doi:10.23919/OCEANS.2015.7404559.

[6] D. Symonds, E. Davis, R. C. Ertekin, Low-power autonomous wave energy capture device for remote sensing and communications applications, in: 2010 IEEE Energy Conversion Congress and Exposition, 2010, pp. 2392–2396. doi:10.1109/ECCE.2010.5617902.

[7] M. Carandell, D. M. Toma, M. Carbonell, J. del Rio, M. Gasulla, Design and testing of a kinetic energy harvester embedded into an oceanic drifter, IEEE Sensors Journal 20 (23) (2020) 13930–13939. doi:10.1109/JSEN.2020.2976517.

[8] M. Carandell, J. Tichy, J. Smilek, D. M. Toma, M. Gasulla, J. del Río, Z. Hadas, Electromagnetic rolling mass wave energy harvester for oceanic drifter applications, The European Physical Journal Special Topics (Mar. 2022). doi:10.1140/epjs/s11734-022-00499-5.
URL https://doi.org/10.1140/epjs/s11734-022-00499-5

[9] G. Shi, D. Tong, Y. Xia, S. Jia, J. Chang, Q. Li, X. Wang, H. Xia, Y. Ye, A piezoelectric vibration energy harvester for multi-directional and ultra-low frequency waves with magnetic coupling driven by rotating balls, Applied Energy 310 (2022) 118511. doi:https://doi.org/10.1016/j.apenergy.2021.118511.

[10] Y. Li, Q. Guo, M. Huang, X. Ma, Z. Chen, H. Liu, L. Sun, Study of an electromagnetic ocean wave energy harvester driven by an efficient swing body toward the self-powered ocean buoy application, IEEE Access 7 (2019) 129758–129769. doi:10.1109/ACCESS.2019.2937587.

[11] R. Chumbinho, J. Pinto, R. Silva, J. D. Rio, P. Gonçalves, A. Sousa, F. Pedrera, M. Lucas, N. Almeida, R. Neta, A. Rocha, S. Gomes, D. Lozano, J. António, The WAVY Drifters and Their Role in Ocean Observation, in: 9th EuroGOOS International conference, Advances in Operational Oceanography: Expanding Europe´s Observing and Forecasting Capacity, Shom and Ifremer and EuroGOOS AISBL, Brest, France, 2021, pp. 458–466.

[12] P.-M. Poulain, R. Gerin, E. Mauri, R. Pennel, Wind effects on drogued and undrogued drifters in the eastern mediterranean, Journal of At-

mospheric and Oceanic Technology 26 (6) (2009) 1144–1156. doi:10.1175/2008JTECHO618.1.

[13] J. Meyerjürgens, T. H. Badewien, S. P. Garaba, J.-O. Wolff, O. Zielinski, A state-of-the-art compact surface drifter reveals pathways of floating marine litter in the german bight, Frontiers in Marine Science 6 (2019) 58. doi:10.3389/fmars.2019.00058.
URL https://www.frontiersin.org/article/10.3389/fmars.2019.00058

[14] C. Rodrigues, M. Ramos, R. Esteves, J. Correia, D. Clemente, F. Gonçalves, N. Mathias, M. Gomes, J. Silva, C. Duarte, T. Morais, P. Rosa-Santos, F. Taveira-Pinto, A. Pereira, J. Ventura, Integrated study of triboelectric nanogenerator for ocean wave energy harvesting: Performance assessment in realistic sea conditions, Nano Energy 84 (2021) 105890. doi:https://doi.org/10.1016/j.nanoen.2021.105890.

[15] H. Joe, H. Roh, H. Cho, S.-C. Yu, Development of a flap-type mooringless wave energy harvesting system for sensor buoy, Energy 133 (2017) 851–863. doi:https://doi.org/10.1016/j.energy.2017.05.143.

[16] R. Lumpkin, M. Pazos, Measuring surface currents with surface velocity program drifters: the instrument, its data, and some recent results, Lagrangian analysis and prediction of coastal and ocean dynamics 39 (2007) 67.

[17] S. J. Beatty, M. Hall, B. J. Buckham, P. Wild, B. Bocking, Experimental and numerical comparisons of self-reacting point absorber wave energy converters in regular waves, Ocean Engineering 104 (2015) 370–386.

[18] L. Berggren, M. Johansson, Hydrodynamic coefficients of a wave energy device consisting of a buoy and a submerged plate, Applied Ocean Research 14 (1) (1992) 51–58.

[19] H. Eidsmoen, Hydrodynamic parameters for a two-body axisymmetric system, Applied Ocean Research 17 (2) (1995) 103–115.

[20] S. Olaya, J.-M. Bourgeot, M. E. H. Benbouzid, Hydrodynamic coefficient computation for a partially submerged wave energy converter, IEEE Journal of Oceanic Engineering 40 (3) (2014) 522–535.

[21] C. Liang, L. Zuo, On the dynamics and design of a two-body wave energy converter, Renewable energy 101 (2017) 265–274.

[22] E. S. Hadi, M. Iqbal, A. Wibawa, O. Kurdi, et al., Experimental studies of interaction forces that affect the position of vertical plates on oscillating heave plates with cylindrical bodies in regular waves., International Journal of Renewable Energy Development 9 (1) (2020).

[23] Y. Du, M. Cheng, K. T. Chau, X. Liu, F. Xiao, W. Zhao, K. Shi, L. Mo, Comparison of linear primary permanent magnet vernier machine and linear vernier hybrid machine, IEEE Transactions on Magnetics 50 (11) (2014) 10–13. doi:10.1109/TMAG.2014.2317805.

[24] J. A. García-Alzórriz, J. Grau, R. Córdoba, J. Muela, A novel double-sided flat rectangular linear permanent magnets synchronous generator for sea wave energy application, ELECO 2011 - 7th International Conference on Electrical and Electronics Engineering (2011) 248–252.

[25] J. Zhang, H. Yu, Q. Chen, M. Hu, L. Huang, Q. Liu, Design and Experimental Analysis of AC Linear Generator with Halbach PM Arrays for Direct-Drive Wave Energy Conversion, IEEE Transactions on Applied Superconductivity 24 (3) (2014) 11–14. doi:10.1109/TASC.2013.2292640.

[26] J. Du, D. Liang, L. Xu, Q. Li, Modeling of a linear switched reluctance machine and drive for wave energy conversion using matrix and tensor approach, IEEE Transactions on Magnetics 46 (6) (2010) 1334–1337. doi:10.1109/TMAG.2010.2041041.

[27] S. E. Rauch, L. J. Johnson, Design principles of flux-switch alternators [includes discussion], Transactions of the American Institute of Electrical Engineers. Part III: Power Apparatus and Systems 74 (3) (1955) 1261–1268. doi:10.1109/AIEEPAS.1955.4499226.

[28] E. Hoang, H. BEN AHMED, J. Lucidarme, Switching flux permanent magnet polyphased synchronous machines, in: EPE 97, Trondheim, Norway, 1997.
URL https://hal.archives-ouvertes.fr/hal-00533004

[29] J. T. Chen, Z. Q. Zhu, Winding configurations and optimal stator and rotor pole combination of flux-switching pm brushless ac machines, IEEE Transactions on Energy Conversion 25 (2) (2010) 293–302. doi:10.1109/TEC.2009.2032633.

[30] C. Wang, J. Shen, L. Wang, K. Wang, A novel permanent magnet flux-switching linear motor, in: 2008 4th IET Conference on Power Electronics, Machines and Drives, IET, 2008, pp. 116–119.

[31] L. Huang, H. Yu, M. Hu, J. Zhao, Z. Cheng, A novel flux-switching permanent-magnet linear generator for wave energy extraction application, IEEE Transactions on Magnetics 47 (5) (2011) 1034–1037. doi:10.1109/TMAG.2010.2093509.

[32] J. Wang, W. Wang, R. Clark, K. Atallah, D. Howe, A tubular flux-switching permanent magnet machine, Journal of Applied Physics 103 (7) (2008) 103–106. doi:10.1063/1.2830541.

[33] Z. Zhu, X. Chen, J. Chen, D. Howe, J. Dai, Novel linear flux-switching permanent magnet machines, in: 2008 International Conference on Electrical Machines and Systems, IEEE, 2008, pp. 2948–2953.

[34] D. Lo, H. Lawali Ali, Y. Amara, G. Barakat, F. Chabour, Computation of cogging force of a linear tubular flux switching permanent magnet machine using a hybrid analytical modeling, 2018 IEEE International Magnetic Conference, INTERMAG 2018 54 (11) (2018). doi:10.1109/INTMAG.2018.8508771.

[35] J. Wang, W. Wang, K. Atallah, D. Howe, Design considerations for tubular flux-switching permanent magnet machines, IEEE Transactions on Magnetics 44 (11 PART 2) (2008) 4026–4032. doi:10.1109/TMAG.2008.2002773.

[36] J. Harms, T. Kern, Proof of concept validation of a swimming multi sensor platform for in-situ ocean monitoring, in: SMSI 2021 - Sensors and Instrumentation, AMA Service GmbH, Von-Münchhausen-Str. 49, 31515 Wunstorf, Germany, 2021. doi:10.5162/smsi2021/b4.4.
URL https://doi.org/10.5162/smsi2021/b4.4

[37] J. Harms, T. A. Kern, Self-sufficient modular multi sensor platform for remote long time ocean observations in large quantities (Mar. 2021).

doi:10.5194/egusphere-egu21-93.
URL https://doi.org/10.5194/egusphere-egu21-93

[38] G. Novelli, C. M. Guigand, C. Cousin, E. H. Ryan, N. J. M. Laxague, H. Dai, B. K. Haus, T. M. Özgökmen, A biodegradable surface drifter for ocean sampling on a massive scale, Journal of Atmospheric and Oceanic Technology 34 (11) (2017) 2509 – 2532. doi:10.1175/JTECH-D-17-0055.1.
URL https://journals.ametsoc.org/view/journals/atot/34/11/jtech-d-17-0055.1.xml

[39] L. Dostal, E. Kreuzer, Probabilistic approach to large amplitude ship rolling in random seas, Proceedings of the Institution of Mechanical Engineers, Part C: Journal of Mechanical Engineering Science 225 (10) (2011) 2464–2476.

[40] L. Dostal, E. Kreuzer, N. Sri Namachchivaya, Non-standard stochastic averaging of large-amplitude ship rolling in random seas, Proceedings of the Royal Society A: Mathematical, Physical and Engineering Sciences 468 (2148) (2012) 4146–4173.

[41] O. Farrok, M. R. Islam, M. R. Sheikh, Y. G. Guo, J. G. Zhu, Design and Analysis of a Novel Lightweight Translator Permanent Magnet Linear Generator for Oceanic Wave Energy Conversion, IEEE Transactions on Magnetics 53 (11) (2017) 10–13. doi:10.1109/TMAG.2017.2713770.

[42] D. S. Lo, Y. Amara, G. Barakat, F. Chabour, Cogging force reduction in linear tubular flux switching permanent-magnet machines, Open Physics 16 (1) (2018) 243–248. doi:doi:10.1515/phys-2018-0035.
URL https://doi.org/10.1515/phys-2018-0035

[43] L. Huang, H. Yu, M. Hu, C. Liu, B. Yuan, Research on a tubular primary permanent-magnet linear generator for wave energy conversions, IEEE Transactions on Magnetics 49 (5) (2013) 1917–1920. doi:10.1109/TMAG.2013.2239981.

[44] O. Farrok, M. R. Islam, M. R. I. Sheikh, W. Xu, A new optimization methodology of the linear generator for wave energy conversion systems, in: 2016 IEEE International Conference on Industrial Technology (ICIT), 2016, pp. 1412–1417. doi:10.1109/ICIT.2016.7474965.

[45] R. H. Byrd, M. E. Hribar, J. Nocedal, An interior point algorithm for large-scale nonlinear programming, SIAM Journal on Optimization 9 (4) (1999) 877–900.

[46] J. R. Barber, Contact mechanics, Vol. 250, Springer, 2018.

[47] W. Goldsmith, Impact: The theory and physical behavior of colliding solids, E. Arnold, 1960.

[48] J. N. Newman, Marine hydrodynamics, The MIT press, 2018.

[49] A. Williams, W. Li, K.-H. Wang, Water wave interaction with a floating porous cylinder, Ocean Engineering 27 (1) (2000) 1–28.

[50] Y. Zheng, Y. Shen, Y. You, B. Wu, L. Rong, Hydrodynamic properties of two vertical truncated cylinders in waves, Ocean engineering 32 (3-4) (2005) 241–271.

Appendix 1 Hydrodynamic Forces

Assuming an unsteady, irrotational flow and using potential flow theory, the pressure p can be computed from Bernoulli's equation [48]

$$p(x,y,z,t) = -\rho\frac{\partial\Phi(x,y,z,t)}{\partial t} - \rho g z, \tag{23}$$

whereby Φ is the velocity potential, ρ is the density of the water and g is the acceleration due to gravity. In Eq. (23), a linearization in Φ has been done.

In the following, only regular waves are considered. For this, the water displacement of amplitude A, frequency ω and wave number k_e are given by

$$\eta(x,t) = \mathrm{Re}\{A\exp(\mathrm{i}(k_\mathrm{e}x - \omega t))\} \quad \text{with } \omega^2 = k_\mathrm{e} g \tanh(k_\mathrm{e} h). \tag{24}$$

Considering only the vertical motion of the buoy and plate, the overall velocity potential Φ can be written in the form [20]

$$\begin{aligned}\Phi(x,y,z,t) = \mathrm{Re}\{&A[\phi_0(x,y,z) + \phi_7(x,y,z)]\exp(-\mathrm{i}\omega t)\\ &+ (-\mathrm{i}\omega)(\mathcal{A}_1\varphi_{3,1}(x,y,z) + \mathcal{A}_2\varphi_{3,2}(x,y,z))\exp(-\mathrm{i}\omega t)\}.\end{aligned} \tag{25}$$

Thereby, ϕ_0 is the incident potential of the wave, which is not disturbed by the mechanical system; ϕ_7 is the scattering potential that has been introduced

in order to represent the disturbances of the incident waves by the fixed system; $\varphi_{3,1}$ and $\varphi_{3,2}$ are the respective radiation potentials, which represent the velocity potential of rigid body motion with unit amplitude in the vertical direction in the absence of incident waves; $\mathcal{A}_1$ and $\mathcal{A}_2$ are the respective complex amplitudes of the vertical motion of the buoy and plate:

$$\xi_k(x,t) = \mathrm{Re}\{\mathcal{A}_k \exp(-\mathrm{i}\omega t)\},\ k \in \{1,2\}. \tag{26}$$

Plugging Eq. (23), Eq, (25) and Eq. (26) into Eq. (1) results in

$$\begin{aligned} m_1\ddot{\xi_1} =& \mathrm{Re}\{Af_1 \exp(-i\omega t)\} - \mu_{1,1}\ddot{\xi_1} - \lambda_{1,1}\dot{\xi_1} - \mu_{2,1}\ddot{\xi_2} - \lambda_{2,1}\dot{\xi_2} \\ & - \iint_{S_1} \rho g z n_3 \mathrm{d}S - m_1 g + F_\mathrm{s} + F_\mathrm{d} - \lambda_{\mathrm{exp},1}\dot{\xi_1}, \\ m_2\ddot{\xi_2} =& \mathrm{Re}\{Af_2 \exp(-\mathrm{i}\omega t)\} - \mu_{2,2}\ddot{\xi_2} - \lambda_{2,2}\dot{\xi_2} - \mu_{1,2}\ddot{\xi_1} - \lambda_{1,2}\dot{\xi_1} \\ & - \iint_{S_2} \rho g z n_3 \mathrm{d}S - m_2 g - F_\mathrm{s} - F_\mathrm{d} - \lambda_{\mathrm{exp},2}\dot{\xi_2}, \end{aligned}$$

whereby the excitation force f_k has been defined as

$$f_k := \mathrm{i}\omega\rho \iint_{S_k} [\phi_0 + \phi_7] n_3 \mathrm{d}S,\ k \in \{1,2\}. \tag{27}$$

and the added mass coefficients $\mu_{j,k}$ and hydrodynamic damping coefficients $\lambda_{j,k}$ from body k resulting from the motion of body j are given by

$$\mu_{j,k} + \mathrm{i}\frac{\lambda_{j,k}}{\omega} := \rho \iint_{S_k} \varphi_{3,j} n_3 \mathrm{d}S \text{ with } \mu_{j,k}, \lambda_{j,k} \in \mathbb{R},\ j,k \in \{1,2\}. \tag{28}$$

The values of f_k, $\mu_{j,k}$ and $\lambda_{j,k}$ are dependent on the geometry of the system, wave frequency ω and the water depth h, respectively.

Appendix 2 Computation of Hydrodynamic Coefficients

In this following, the approach for the computation of the hydrodynamic coefficients $\mu_{j,k}$, $\lambda_{j,k}$, and f_k is sketched. In order to compute them for cylindrical bodies analytically, the matched eigenfunction method is used. The majority of research works has studied systems, where the radius of the buoy and of the cylindrical plate are the same, see for example [18, 19, 49, 50]. In this paper, we refer to the work of Olaya et al. [20], who have presented

an analytical way to compute the coefficients for different radii of the buoy, plate, and connection rod for the case of heave motion.

In order to compute the values of $\mu_{j,k}$, $\lambda_{j,k}$, and f_k, the velocity potentials ϕ_7, $\varphi_{3,1}$, and $\varphi_{3,2}$ have to be computed, see Eqs. (27) and (28). For the heave motion, they have to satisfy Laplace's equation, a linearized free-surface condition, and the following body boundary conditions

$$\frac{\partial \varphi_{3,k}}{\partial z} = \delta_{j,k}, \ \frac{\partial \phi_7}{\partial z} = -\frac{\partial \phi_0}{\partial z} \ \text{ on } S_j, \tag{29}$$

whereby δ_{jk} is the dirac-delta operator. The incident potential ϕ_0 corresponds to the incoming wave and is assumed to be known.

In order to fulfil all these equations, the water domain is separated into three or four subdomains, depending on the plate radius size. For details, we refer to the work of Olaya et al. [20]. In each subdomain, analytical expressions for the different velocity potentials are obtained using the variable separation method and by expressing them as infinite series of orthogonal functions, which fulfil the different boundary conditions. Thereby, continuity of the overall velocity potential is ensured by means of appropriate transition conditions.